Exploring Structural Changes in Ge-Te Amorphous Films Through Small-Angle Neutron Scattering

Andrea Piarristeguy, Raphaël Escalier, Annie Pradel, Viviana Cristiglio, Gabriel Cuello

applied sciences

MDPI

Article

Exploring Structural Changes in Ge-Te Amorphous Films Through Small-Angle Neutron Scattering

Andrea A. Piarristeguy [1], Raphaël Escalier [1], Annie Pradel [1], Viviana Cristiglio [2] and Gabriel J. Cuello [1,*]

[1] ICGM, Univ. Montpellier, CNRS, ENSCM, 34095 Montpellier, France; andrea.piarristeguy@umontpellier.fr (A.A.P.); raphael.escalier@umontpellier.fr (R.E.); annie_pradel@yahoo.fr (A.P.)
[2] Institut Laue Langevin, 71 Avenue des Martyrs, 38042 Grenoble, France; cristigl@ill.fr
* Correspondence: cuello@ill.fr

Abstract: The structure of the glassy Ge_xTe_{1-x} system, with $x = 0.17, 0.21, 0.28, 0.30$, and 0.45, is studied using the small-angle neutron scattering (SANS) technique. The very-low-momentum-transfer region of the diffractogram exhibits distinct behaviour depending on the germanium content. A similar conclusion is drawn from the analysis of the first diffraction peaks observed at higher angles. This system exhibits three composition regions with distinct behaviours: a first zone of low Ge content (up to about 20–25 at.%), a third zone richer in Ge (from about 30 at.% and above), and a second transitional zone between them. These changes are reflected in the parameters that govern Porod's region, as well as in the region where the first diffraction peaks appear, corroborating previous observations made using other experimental and simulation techniques. Our study provides experimental evidence that could open up new possibilities for conducting simulations using neutron data. The results presented here show that increasing Ge content leads to a strengthening of the intermediate-range order at the expense of a weakening of the short-range order.

Keywords: chalcogenide glasses; SANS; neutron diffraction; short-range order; intermediate-range order; correlation distances

Citation: Piarristeguy, A.A.; Escalier, R.; Pradel, A.; Cristiglio, V.; Cuello, G.J. Exploring Structural Changes in Ge-Te Amorphous Films Through Small-Angle Neutron Scattering. *Appl. Sci.* **2024**, *14*, 11713. https://doi.org/10.3390/app142411713

Academic Editors: Mioara Zagrai and Ramona-Crina Suciu

Received: 6 November 2024
Revised: 2 December 2024
Accepted: 10 December 2024
Published: 16 December 2024

1. Introduction

GeTe-based materials, known for their remarkable phase-change behaviour [1] and thermoelectric [2,3] performance, are widely explored for advanced applications in non-volatile memory devices and energy-harvesting systems. Phase-Change Materials (PCMs) were first conceptualised in the late 1960s, with Stanford Ovshinsky's pioneering work [4] highlighting their potential for data storage applications. These materials exhibit unique properties, such as the ability to switch between crystalline and amorphous states, each with distinct optical and electrical characteristics. The crystalline phase typically shows high electrical conductivity and high optical reflectivity, whereas the amorphous phase has high resistivity and low reflectivity. This transformation, driven by external energy inputs like laser pulses or electrical currents, occurs on the nanosecond scale and is fully reversible [5]. Prominent PCM compositions include telluride-based materials, such as $Ge_2Sb_2Te_5$, $Ge_1Sb_2Te_4$, and GeTe [6–8], which have been widely utilised in optical storage devices like CD-RW, DVD-RW, and Blu-ray Discs due to their fast switching capabilities, durability, and scalability [9].

Current research focuses on advancing PCMs for electrical memory technologies, such as Phase-Change Random-Access Memory (PC-RAM), which offers advantages such as faster speeds, greater energy efficiency, and enhanced durability compared to conventional flash memory. One of the defining characteristics of PCMs is their ability to crystallise rapidly from the amorphous phase, generating a marked contrast in electrical properties between the two states. However, the interaction between the amorphous and crystalline structures remains a critical area of research. These structures must be sufficiently distinct to

ensure the stability of the amorphous phase and reliable data retention at operating temperatures yet topologically similar enough to enable rapid crystallisation within nanoseconds.

Storage density is another crucial aspect of PC-RAM technology. One approach to enhancing storage density is the development of multi-level cells (MLCs) [10], where the resistance of a cell can be precisely adjusted by modulating the volume of its amorphous phase. However, this requires a stable amorphous state with time-independent resistance. A significant challenge in this area is resistance drift [11–13], a phenomenon in which the resistivity of amorphous telluride materials, such as GeTe and $Ge_{0.15}Te_{0.85}$, increases over time, potentially leading to data degradation in MLCs.

During the last decades, different techniques have been used to study the atomic and local structures of amorphous Ge-Te, including the extended X-ray absorption fine structure (EXAFS) at the Ge and Te K-edges [14–16], anomalous X-ray scattering [17], time-of-flight neutron diffraction [18], X-ray absorption fine structure spectroscopy [16], and numerical simulations [19–22]. Previous studies on amorphous Ge_xTe_{1-x} ($0.10 < x \leq 0.50$) films, produced via co-sputtering, have identified three distinct regimes of resistance drift, with notable transitions occurring at approximately 25 at.% and 35 at.% Ge. Ge-rich glasses ($x > 0.25$) exhibit high drift coefficients, with values ranging from 0.13 for $Ge_{0.50}Te_{0.50}$ to ≈0.29 for compositions near the stiffness threshold. In contrast, the drift coefficient decreases with lower Ge content in Ge-poor compositions ($x \leq 0.25$) [23]. These anomalies may result from microstructural or topological changes, although the possibility of phase separation near the critical composition thresholds cannot be ruled out.

Recent structural analyses of co-evaporated or sputtered Ge_xTe_{1-x} ($0.10 < x \leq 0.50$), utilising techniques such as X-ray diffraction and EXAFS combined with reverse Monte Carlo (RMC) modelling, have provided valuable insights into the atomic-scale structure [24–26]. This research has identified two structural singularities at approximately 22–25 at.% and about 33 at.% Ge. The first singularity, at 22–25 at.% Ge, corresponds to the minimum bond variability and homopolar bond fractions, indicating a high level of structural organisation. This behaviour aligns with the flexible-to-rigid transition predicted by rigidity theory, initially proposed by Phillips and Thorpe [27,28]. Experimental evidence supports this interpretation, with maximum values of thermal stability ($\Delta T = T_x - T_g$), where T_x is the temperature of crystallisation onset and T_g the glass transition temperature and the optical band gap (E_g) observed near 22 at.% Ge [27].

The second singularity, occurring at compositions above about 33 at.% Ge, signifies a pronounced trend towards crystallisation, as evidenced by the disappearance of the glass transition temperature (T_g) and a sharp decrease in the crystallisation temperature (T_x). Structurally, this Ge-rich region is marked by increased disorder, reflected in a constant distribution of heteropolar and homopolar bonds, significant bond length variability, and the consistent intensity of the First Sharp Diffraction Peak (FSDP) in the concentration–concentration structure factor [25]. The enhanced Ge-Ge correlations observed at intermediate length scales (∼7.7 Å) in this region further suggest the potential for phase separation.

In this study, we aim to extend the structural investigation of the Ge-Te system by exploring potential rearrangements at the nanometre scale using small-angle neutron scattering (SANS). The objective is to clarify the structural evolution of Ge_xTe_{1-x} amorphous films. Covering a wide range of momentum transfer, we monitored structural changes from large structural units to short-range order (SRO, corresponding to interatomic distances), also covering intermediate-range order (IRO, corresponding to connections and relative orientations of groups of atoms) [29,30]. Within this context, fitting Porod's region [31] in the SANS diffractograms also aims to reveal the topology of the system and to provide insights into its morphology and dimensionality.

2. Materials and Methods

In this work, we studied amorphous films of the Ge_xTe_{1-x} system with $x < 0.5$. The use of films, rather than materials prepared by melt-quenching techniques, is justified

by the inherently limited amorphous domain of this system. Thermal co-evaporation offers a significant advantage by enabling access to a broader amorphous region, making it a more suitable technique for investigating amorphous GeTe mixtures.

The use of the SANS technique offers certain advantages over X-rays. The neutron scattering lengths of Ge (8.185 fm) and Te (5.80 fm) are comparable, allowing a balanced analysis of both elements in the Ge-Te glass structure. This contrasts with X-rays, where the higher atomic number of tellurium (Z = 52) leads to a dominant contribution, overshadowing that of germanium (Z = 32). In X-ray studies, the atomic form factor serves as the equivalent to the neutron scattering length, but its dependence on atomic number makes X-rays less suited for studying systems with significant differences in Z.

2.1. Sample Preparation

Five thick amorphous films with measured compositions of $Ge_{0.17}Te_{0.83}$, $Ge_{0.21}Te_{0.79}$, $Ge_{0.28}Te_{0.72}$, $Ge_{0.30}Te_{0.70}$, and $Ge_{0.45}Te_{0.55}$ were prepared via thermal co-evaporation using a MEB 500 system from Plassys. Microscope slides were employed as substrates. Prior to deposition, the chamber was evacuated to a pressure of 10^{-7} mbar. Germanium pieces (from Goodfellow, Huntingdon, UK, 99.999%) were evaporated by electron beam bombardment, while tellurium pieces (from Sigma-Aldrich, St. Louis, MI, USA, 99.999%) were evaporated from two current-induced heated sources. During deposition, the substrate holder was rotated and heated to approximately 70 °C. The deposition rate for each element was automatically controlled using a thin film deposition controller.

The samples (approximately 150–200 mg) required for the SANS measurements were prepared by scraping the 5–7 µm thick co-evaporated films. This process produces fragments that are primarily two-dimensional, with a thickness equivalent to that of the film and dimensions of 1–2 mm in the other directions. The film compositions were verified using Electron-Probe Micro-Analysis (EPMA) with a CAMECA SX-100 (Paris, France) instrument. The amorphous nature of all as-deposited films was confirmed through X-ray diffraction, performed using a PANalytical XPERT (Almelo, The Netherlands) diffractometer with a Cu (K_α) source for an incident wavelength of $\lambda = 1.5406$ Å.

2.2. Small-Angle Neutron Scattering

The SANS experiments were performed using the small momentum transfer diffractometer D16 at the Institut Laue-Langevin (Grenoble, France) using a wavelength of $\lambda = 4.47$ Å. This provides a high $\Delta Q/Q$ resolution of 1%, suitable for detailed structural analysis. Six detector positions (SANS and WANS configurations) were used to achieve a broad Q-range from 2×10^{-2} Å^{-1} to 2.2 Å^{-1} ($Q = 4\pi/\lambda \sin\theta$, where 2θ is the scattering angle).

The monochromatic neutron beam dimensions at the sample position were defined by slits of 25×5 mm^2 and centred on a cylindrical vanadium sample holder with a 4 mm inner diameter and 66 mm length. This setup ensured the uniform illumination of the sample cell by the neutron beam.

Amorphous Ge_xTe_{1-x} films were placed in the unsealed cylindrical vanadium containers, and the room-temperature diffraction patterns were collected by moving the neutron detector around the sample at a fixed distance. The sample cells were mounted in a rotative sample changer. In addition to the samples, the necessary ancillary measurements were performed, including a vanadium rod (5 mm in diameter), empty cell, and cadmium, all with dimensions closely matching those of the sample.

The resulting 2D data were radially averaged to obtain the scattered intensity $I(Q)$ as a function of Q. Data were corrected by taking into account the empty cell, environmental background, sample transmission, and the thickness of the sample. Additionally, the data were then normalised using a vanadium standard to correct for the non-uniform detector response. This data reduction was carried out using the ILL's LAMP software (https://www.ill.eu/users/support-labs-infrastructure/software-scientific-tools/lamp, accessed on 9 December 2024) [32] and specific routines for SANS experiments.

3. Results

Figure 1 shows the SANS diffractograms recorded at room temperature for all Ge_xTe_{1-x} samples. All the curves display similar behaviour, showing a linear regime (in the log–log plot) in the low-Q region (below 0.1 Å^{-1}) and exhibiting two diffraction peaks in the high-Q region (above 0.3 Å^{-1}): at about 1 Å^{-1} for the FSDP and at about 2 Å^{-1} for the Principal Peak (PP). Despite these similarities, some differences are evident at a glance. The two samples with lower germanium content display nearly the same behaviour in the low-Q region, while the others exhibit much higher intensity and different slopes.

To quantitatively analyse the diffractograms shown in Figure 1, fitting is performed in the range 0.03 to 2.3 Å^{-1} using the following fitting function:

$$f(Q) = \gamma + \alpha\, Q^{-\beta} + \sum_{\text{label=FSDP, PP}} \frac{A_{\text{label}}}{\sqrt{2\pi}\,\sigma_{\text{label}}} \exp\left(-\frac{(Q - Q_{\text{label}})^2}{2\sigma^2_{\text{label}}}\right), \quad (1)$$

where γ is the background. This function has two main contributions: a power-law function to describe the low-Q region (below 0.1 Å^{-1}), also known as Porod's region, and a couple of Gaussian peaks describing the high-Q (or diffraction) region. The α parameter takes into account the intensity of the SANS signal (proportional to the neutron counts per detection channel), and β is the exponent of the power function. For the Gaussian peaks, the parameters are the usual ones: A_{label}, Q_{label}, and σ_{label} (label: FSDP or PP) are the area, the centre, and the standard deviation, respectively. Figure 2 shows the fit corresponding to the $Ge_{0.17}Te_{0.83}$ sample, representing the typical fit for all samples. The resulting parameters from this fitting process are shown in Tables 1 and 2.

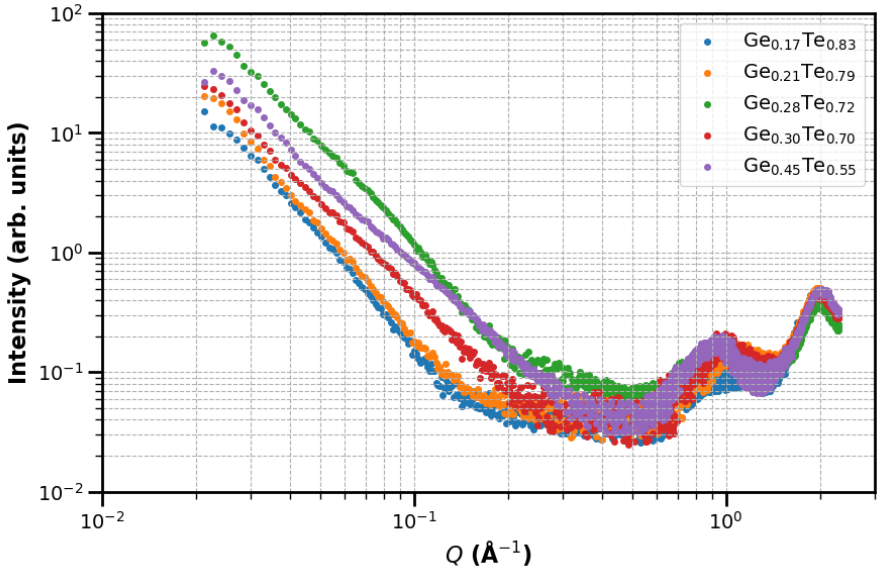

Figure 1. SANS diffractograms as determined on the D16 instrument for the five Ge_xTe_{1-x} samples, with $x = 0.17, 0.21, 0.28, 0.30$, and 0.45.

Table 1. Fitted parameters of the power-law function, Equation (1), for the Ge_xTe_{1-x} samples in the low-Q region. The numbers in parentheses represent the uncertainties affecting the last two significant digits of the tabulated values.

$x =$	0.17	0.21	0.28	0.30	0.45
$\alpha/10^{-5}$	9.93 (29)	9.15 (26)	206.6 (3.2)	85.2 (1.8)	95.5 (1.9)
β	3.1689 (88)	3.2487 (86)	2.7587 (47)	2.6770 (64)	2.7897 (60)
$\gamma/10^{-2}$	2.52 (17)	3.89 (14)	2.40 (58)	2.46 (21)	7.25 (20)

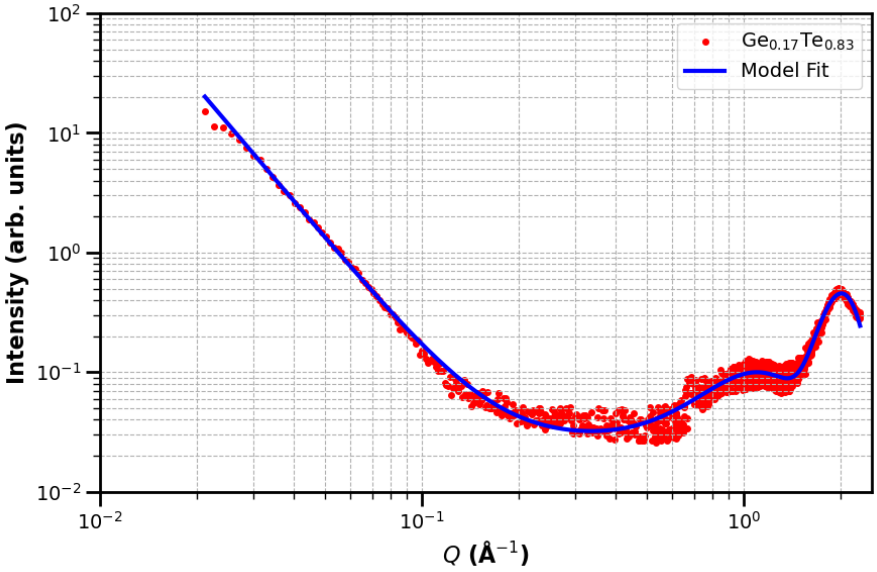

Figure 2. The fit of the model given by Equation (1) to the $Ge_{0.17}Te_{0.83}$ sample data. The fitted parameters and their optimised values are shown in Tables 1 and 2.

The strong variation in the α and β parameters shown in Table 1 allows for a clear separation of the five samples into two distinct groups: up to 22 at.% and above 30 at.% Ge, with the sample with 28 at.% Ge being in a transition zone. The most relevant parameter in Porod's region is the exponent β, which is shown in Figure 3.

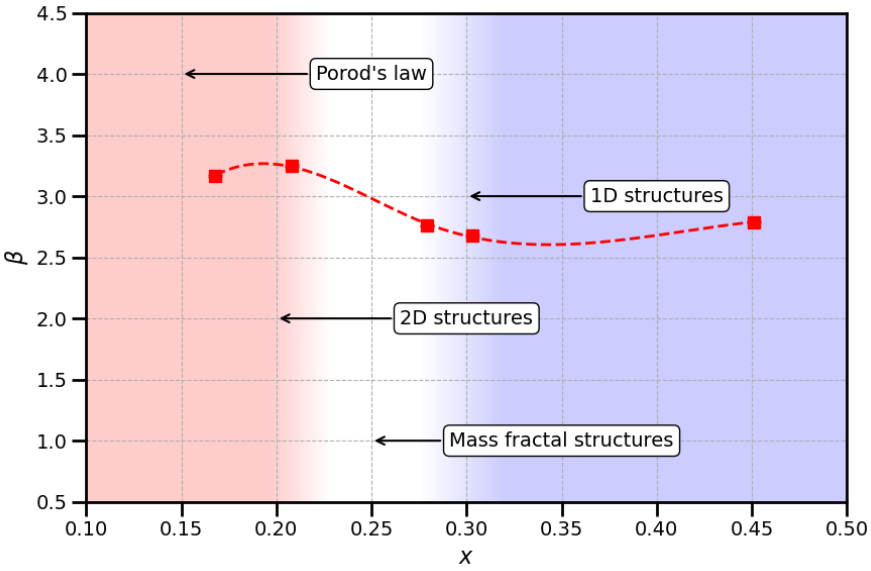

Figure 3. The power-law exponent β, as obtained from the fit of the low-Q region, is plotted as a function of Ge content x. The dashed line is a smoothed spline that only serves as a guide for the eye. The red-, white-, and blue-shaded areas correspond to the different zones observed as a function of the Ge content. Labels and arrows indicate the expected values of β for typical structures or behaviours.

When the exponent is 4, this power law is known as Porod's law [33] and typically describes a surface-dominated scattering from a well-defined structure, such as a large aggregate or particle with smooth interfaces.

Table 2. Fitted parameters for the Ge_xTe_{1-x} samples in the high-Q region, i.e., the Gaussian parameters in Equation (1). The areas A are in arbitrary units, while peak positions Q and widths σ are in $Å^{-1}$. Correlation distances D (see text for details) are in Å. The numbers in parentheses represent the uncertainties affecting the last two significant digits of the tabulated values.

$x = 0.17$	FSDP	PP	$x = 0.21$	FSDP	PP
A	0.0576 (28)	0.2652 (19)	A	0.0663 (19)	0.2627 (19)
Q	1.0907 (66)	2.0126 (13)	Q	1.1040 (39)	2.0070 (14)
σ	0.310 (11)	0.2464 (16)	σ	0.2555 (57)	0.2447 (18)
D	8.62 (30)	10.83 (7)	D	10.44 (23)	10.90 (8)
$x = 0.28$	FSDP	PP			
A	0.0839 (83)	0.2150 (71)			
Q	0.986 (13)	2.0156 (54)			
σ	0.274 (19)	0.2685 (74)			
D	9.74 (66)	9.94 (27)			
$x = 0.30$	FSDP	PP	$x = 0.45$	FSDP	PP
A	0.0759 (23)	0.2805 (30)	A	0.0308 (16)	0.2365 (36)
Q	1.0188 (33)	2.0174 (20)	Q	0.9340 (44)	2.0354 (29)
σ	0.2294 (48)	0.2734 (27)	σ	0.1269 (57)	0.2349 (35)
D	11.53 (24)	9.76 (10)	D	21.03 (94)	11.36 (17)

4. Discussion

For the sake of clarity, we discuss the two regions observed in the Q-scale separately: Porod's and the diffraction regions.

4.1. Low-Q Region: Porod's Region

In Porod's region [31], the scattering pattern is dominated by the interfaces between different phases or components within a sample, such as particles or pores in a material. The power law in Equation (1) describes the decay of the scattering intensity, which is related to the size and shape of the scattering entities. This region provides vital information about the surface and structural characteristics of the scattering objects.

In this region, the main parameter is the exponent β, which is critical for interpreting the structural properties of the sample. When the exponent is 4, this power law is known as Porod's law [33] and typically describes a surface-dominated scattering from a well-defined structure, such as a large aggregate or particle with smooth interfaces. A value of 3 suggests a situation where the scattering arises from more complex geometries, such as rod-like or cylindrical structures. In contrast, a value of 2 often corresponds to scattering from mass fractals, where the scatterers are distributed in space but not necessarily in a uniform way.

The values in Table 1 already indicated two distinct groups of samples, and Figure 3 now clearly highlights this. Thus, in line with the discussion in the Introduction, the composition range is divided into three compositional zones: the first up to ≈22 at.% Ge (shaded in red), a second transitional region between ≈22 at.% and ≈30 at.% (white in the plot), and a third above ≈30 at.% (shaded in blue). The $Ge_{0.28}Te_{0.72}$ sample is in the second zone, a transition regime where the fitted parameters may present strong variations. For this sample, the exponent β is in line with the exponents observed for the Ge-rich samples.

The analysis of the scattering exponent as a function of increasing Ge content reveals a decrease from 3.25 to 2.75, corresponding to a 15% reduction. This behaviour suggests that the Ge_xTe_{1-x} system exhibits characteristics of both fractal-like structures and complex geometries. Specifically, this range of exponents indicates that the scattering is influenced by structures combining multiple dimensionalities. An exponent approaching 3 reflects a system with a significant surface area, potentially associated with elongated or rod-like

features, whereas values closer to 2 indicate a degree of fractality. This variation in interface types suggests that the geometry becomes increasingly complex as the Ge content increases.

4.2. High-Q Region: Diffraction Region

The diffraction region starts at about 0.3 $Å^{-1}$, where we observe two diffraction peaks, as shown in Figure 2. By analysing the dependence of the peak parameters on the Ge content x, we observe several trends in the high-Q region.

4.2.1. Peak Positions

The first peak (FSDP), located at 1 $Å^{-1}$, corresponds to IRO in the glass structure. Its position in reciprocal space relates to a longer characteristic distance in real space ($2\pi/Q_{FSDP} \approx 6.28$ Å). The overall decrease of about 15% in this peak's position as the germanium content increases from $x \approx 0.2$ to $x \approx 0.30$ (red symbols in Figure 4) indicates an expansion or modification of the intermediate atomic arrangement. This expansion is much more noticeable when x approaches 0.50. The fact that the intensity of this peak does not change significantly implies that, while the connectivity is being altered, the basic intermediate structural bonds remain relatively intact in terms of their overall number or density. From the perspective of dividing the composition range into three zones, we can say that the position of the FSDP increases in the first zone, whereas it decreases in the third zone.

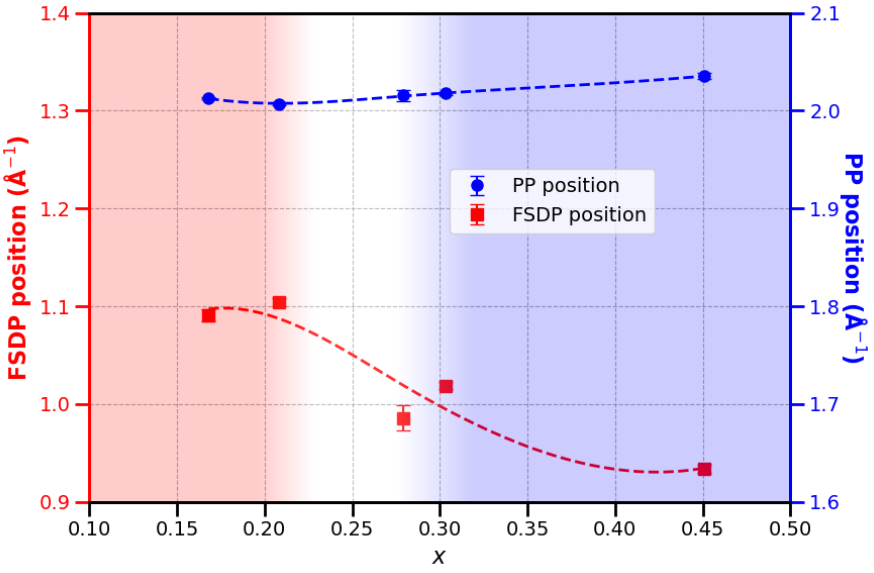

Figure 4. Positions of the FSDP (left scale) and PP (right scale) as a function of the Ge content x. Dashed lines are smoothed splines that only serve as a guide for the eye. The red-, white-, and blue-shaded areas correspond to the different zones observed as a function of the Ge content.

The second peak (PP), at approximately 2 $Å^{-1}$, corresponds to SRO. This peak relates to a shorter characteristic distance in real space compared to the first peak ($2\pi/Q_{PP} \approx 3.14$ Å). The slight increase in the position of this peak, albeit 6 times less than the decrease in the FSDP, may suggest a gradual adjustment in the short-range structural arrangement as germanium is added. This is consistent with observations from simulations of partial correlations using the RMC method [24]. These simulations show that Ge-Ge distances are 5% shorter than Ge-Te distances, which explains the shift in the PP towards higher Q values. Again, from the perspective of compositional zoning, we observe that in the first zone, the position of this peak remains almost unchanged, consistent with RMC simulations, which indicate that only Ge-Te bonds are present for these compositions in the PP. In contrast, in zone 3, the increasing presence of Ge-Ge bonds causes a shift in the reciprocal space position towards higher values.

To finish with the peak positions, it is worth noticing the opposite behaviour of the two peaks: when the FSDP moves to lower positions, the PP moves to higher positions, and vice versa.

4.2.2. Peak Widths

Examining the widths of the diffraction peaks enables an estimation of the degree of order across various length scales. The peak width ΔQ is determined as the full width at half maximum (FWHM), which, for a Gaussian function, corresponds to $\Delta Q = 2\sqrt{2\ln 2}\,\sigma \approx 2.35\,\sigma$. The characteristic distance of ordering in the system is given by $D = 2\pi/\Delta Q$, which represents the extent of the order attributed to the corresponding peak.

The correlation distance associated with the FSDP, initially around 9 Å (in zone 1) and increasing by more than 100% in zone 3 (Figure 5), reflects an enhancement in IRO. This considerable increase suggests that, with higher Ge content, the intermediate atomic ordering extends further, as if clusters or atomic groups are achieving greater spatial coherence or connectivity. This likely indicates that germanium is reinforcing or stabilising the network structure, possibly through the formation of Ge-Te or Ge-Ge clusters or similar motifs that persist over longer ranges.

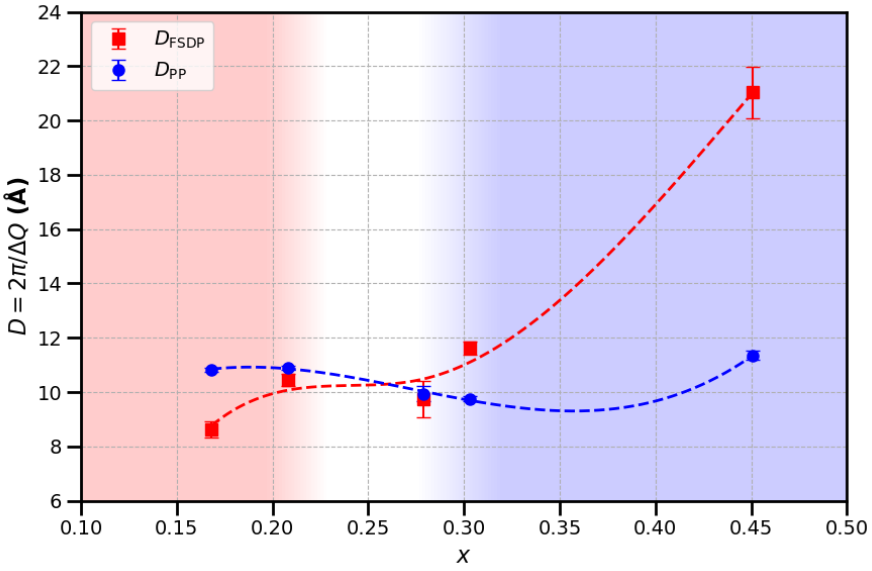

Figure 5. Correlation distances corresponding to the FSDP and PP as a function of Ge content x. Dashed lines are smoothed splines that only serve as a guide for the eye. The red-, white-, and blue-shaded areas correspond to the different zones observed as a function of the Ge content.

For the PP, representing SRO, the correlation distance is more or less constant at about 11 Å for any germanium content (Figure 5). This implies that the initial ordering is retained as more germanium is added. The constancy in the correlation distance for the second peak points to a weakening of SRO with respect to the IRO. That is, as Ge is added, the short-range connections are maintained, possibly breaking down the previously existing Te-rich network in favour of longer, Ge-influenced connections. This provides experimental confirmation of RMC results [24], showing that the addition of Ge causes a gradual transition from a fully ordered SRO model to a disordered one. The huge difference in correlation distance for each peak implies that the glass is evolving to a structure with predominant intermediate-range domains.

By studying both regions (low and high Q), we reach the same conclusion: there are three zones of composition (see the shaded areas in Figures 3–5), with changes occurring in both SRO and IRO. This conclusion is also supported by the shoulder that the diffractogram of the sample with $x = 0.45$ presents at about 0.1 Å^{-1}; the corresponding distance related

to this "peak" is $2\pi/0.1$ Å$^{-1} \approx 62$ Å, a value that is in line with the general trend observed in glassy systems with chemical ordering [34].

5. Conclusions

Using the SANS technique, five samples of the Ge_xTe_{1-x} system were studied, with the aim of obtaining experimental confirmation of effects observed through other experimental and simulation techniques. A range of germanium content, specifically $x < 0.50$, was selected where structural changes were anticipated. The main and most evident conclusion is the confirmation of the existence of three compositional zones, with a central transition zone bridging the low- and high-Ge content zones.

Fitting Porod's region in the SANS part of the diffractograms reveals that the system exhibits a complex topology, possibly of a fractal nature. Further exploration of the morphology and dimensionality within the Ge_xTe_{1-x} system could offer additional insights into the mechanisms underlying the observed scattering behaviour. The intensity patterns in the diffraction region suggest that the Ge_xTe_{1-x} glass system undergoes significant atomic structural changes as the germanium content increases. This observation is consistent with the fact that, within the range of compositions studied here, the Ge-rich mixtures exhibit PCM properties.

The trends in the correlation distances indicate that, with increasing Ge content, the glass structure shifts towards a state where IRO becomes more stabilised, while SRO is somewhat relatively diminished. The difference between these correlation distances (Figure 5) suggests a restructuring process that strengthens the intermediate order at the expense of short-range connectivity.

This delicate balance between short- and intermediate-range structures likely influences the material's overall properties, and further studies could provide deeper insights into how these structural variations impact its use across fields like optics and electronics. The interplay between enhanced intermediate-range ordering and a reduced short-range order may significantly affect macroscopic properties such as density, rigidity, and thermal stability, offering valuable guidance for tailoring glass structures to suit specific applications.

This work highlights the usefulness of neutron diffraction in complementing results obtained from X-rays, particularly regarding the intensity of the FSDP. For example, X-ray data recently employed in RMC simulations [24] barely show the presence of this peak, whereas, in the case of neutrons, it becomes significantly more pronounced. Our study provides experimental evidence that could, in the future, open new avenues for simulations using neutron data and potentially for simulations integrating data from both probes simultaneously. Achieving this would require extending the study to higher momentum transfer values, enabling more precise conclusions about the structural properties.

Author Contributions: Conceptualisation, A.A.P., A.P. and G.J.C.; methodology, G.J.C.; sample preparation, R.E.; laboratory experiments, R.E. and A.A.P.; SANS experiments, A.A.P., R.E., V.C. and G.J.C.; formal analysis, G.J.C.; investigation, A.A.P. and A.P.; data curation, V.C.; writing—original draft preparation, G.J.C.; writing—review and editing, A.A.P. and G.J.C. All authors have read and agreed to the published version of the manuscript.

Funding: This research received no external funding.

Institutional Review Board Statement: Not applicable.

Informed Consent Statement: Not applicable.

Data Availability Statement: Publicly available datasets were analyzed in this study. This data can be found here: Experiment 6-05-990, Institut Laue-Langevin (2017), https://doi.org/10.5291/ILL-DATA.6-05-990 (accessed on 23 November 2024).

Acknowledgments: We are grateful to the ILL for providing neutron beam time (https://doi.org/10.5291/ILL-DATA.6-05-990, accessed on 23 November 2024).

Conflicts of Interest: The authors declare no conflicts of interest.

Abbreviations

The following abbreviations are used in this manuscript:

CD-RW	Compact Disc ReWritable
CNRS	Conseil National de la Recherche Scientifique
DVD-RW	Digital Versatile Disc ReWritable
ENSCM	École Nationale Supérieure de Chimie de Montpellier
EPMA	Electron-Probe Micro-Analysis
EXAFS	Extended X-ray absorption fine structure
FSDP	First Sharp Diffraction Peak
FWHM	Full width at half maximum
ICGM	Institut Charles Gerhardt Montpellier
ILL	Institut Laue Langevin
IRO	Intermediate-range order
LAMP	Large Array Manipulation Program
MLC	Multi-level cell
PC-RAM	Phase-Change Random-Access Memory
PCM	Phase-Change Materials
PP	Principal Peak
RMC	Reverse Monte Carlo
SANS	Small-angle neutron scattering
SRO	Short-range order
WANS	Wide-Angle Neutron Scattering

References

1. Noé, P.; Vallée, C.; Hippert, F.; Fillot, F.; Raty, J.-Y. Phase-change materials for non-volatile memory devices: From technological challenges to materials science issues. *Semicond. Sci. Technol.* **2018**, *33*, 013002. [CrossRef]
2. Nandihall, N. Thermoelectric films and periodic structures and spin Seebeck effect systems: Facets of performance optimization. *Mater. Today Energy* **2022**, *25*, 100965. [CrossRef]
3. Hong, M.; Chen, Z.-G. Chemistry in Advancing Thermoelectric GeTe Materials. *Acc. Chem. Res.* **2022**, *55*, 3178. [CrossRef] [PubMed]
4. Ovshinsky, S.R. Reversible Electrical Switching Phenomena in Disordered Structures. *Phys. Rev. Lett.* **1968**, *21*, 1450. [CrossRef]
5. Bruns, G.; Merkelbach, P.; Schlockermann, C.; Salinga, M.; Wuttig, M.; Happ, T.D.; Philipp, J.B.; Kund, M. Nanosecond switching in GeTe phase change memory cells. *Appl. Phys. Lett.* **2009**, *95*, 043108. [CrossRef]
6. Wuttig, M. Towards a universal memory? *Nat. Mater.* **2005**, *4*, 265. [CrossRef]
7. Yamada, N. Erasable Phase-Change Optical Materials. *Mater. Res. Soc. Bull.* **1996**, *21*, 48. [CrossRef]
8. Noé, P.; Hippert, F. *Phase Change Memory*; Redaelli, A., Ed.; Springer: Cham, Switzerland , 2018; pp. 125–179.
9. Wuttig, M.; Yamada, N. Phase-change materials for rewriteable data storage. *Nat. Mater.* **2007**, *6*, 824. [CrossRef] [PubMed]
10. Wang, J.; Dong, X.; Sun, G.; Niu, D.; Xie, Y. Energy-efficient multi-level cell phase-change memory system with data encoding. In Proceedings of the IEEE 29th International Conference on Computer Design (ICCD), Amherst, MA, USA, 9–12 October 2011; pp. 175–182.
11. Karpov, I.V.; Mitra, M.; Kau, D.; Spadini, G.; Kryukov, Y.A.; Karpov, V.G. Fundamental drift of parameters in chalcogenide phase change memory. *J. Appl. Phys.* **2007**, *102*, 124503. [CrossRef]
12. Noé, P.; Sabbione, C.; Castellani, N.; Veux, G.; Navarro, G.; Sousa, V.; Hippert, F.; d'Acapito, F. Structural change with the resistance drift phenomenon in amorphous GeTe phase change materials' thin films. *J. Phys. D Appl. Phys.* ***2016***, *49*, 035305. [CrossRef]
13. Pries, J.; Stenz, C.; Schäfer, L.; Gutsche, A.; Wei, S.; Lucas, P.; Wuttig, M. Resistance Drift Convergence and Inversion in Amorphous Phase Change Materials. *Adv. Funct. Mater.* **2022**, *32*, 2207194. [CrossRef]
14. Maeda, Y.; Wakagi, M. Ge K-Edge Extended X-Ray Absorption Fine Structure Study of the Local Structure of Amorphous GeTe and the Crystallization. *Jpn. J. Appl. Phys.* **1991**, *30*, 101. [CrossRef]
15. Hirota, K.; Nagino, K.; Ohbayashi, G. Local structure of amorphous GeTe and PdGeSbTe alloy for phase change optical recording. *J. Appl. Phys.* **1997**, *82*, 65. [CrossRef]
16. Sen, S.; Joshi, S.; Aitken, B.G.; Khalid, S. Atomic structure and chemical order in binary Ge–Te and As–Te glasses: A Te K-edge X-ray absorption fine structure spectroscopic study. *J. Non-Cryst. Solids* **2008**, *354*, 4620. [CrossRef]
17. Stellhorn, J.R.; Hosokawa, S.; Pilgrim, W.-C.; Blanc, N.; Boudet, N.; Tajiri, H.; Kohara, S. Short- and intermediate-range order in amorphous GeTe. *Phys. Status Solidi B* **2016**, *253*, 1038. [CrossRef]
18. Kameda, Y.; Uemura, O.; Usuki, T. Time-of-Flight Neutron Diffraction Study of Amorphous and Liquid Ge–Te Alloys. *Mater. Trans.* **1996**, *37*, 1655. [CrossRef]

19. Stellhorn, J.R.; Hosokawa, S.; Kaiser, B.; Kimura, K.; Boudet, N.; Blanc, N.; Tajiri, H.; Kohara, S.; Pilgrim, W.-C. The structure of the amorphous $(GeTe)_{1-x}(Sb_2Te_3)_x$ system and implications for its phase-change properties. *Z. Phys. Chem.* **2021**, *235*, 141. [CrossRef]
20. Akola, J.; Jones, R.O. Structural phase transitions on the nanoscale: The crucial pattern in the phase change materials $Ge_2Sb_2Te_5$ and GeTe. *Phys. Rev. B* **2007**, *76*, 235201. [CrossRef]
21. Gunasekera, K.; Boolchand, P.; Micoulaut, M. Effect of mixed Ge/Si cross-linking on the physical properties of amorphous Ge-Si-Te networks. *J. Appl. Phys.* **2014**, *115*, 164905. [CrossRef]
22. Bouzid, A.; Massobrio, C.; Boero, M.; Ori, G.; Sykina, K.; Furet, E. Role of the van der Waals interactions and impact of the exchange-correlation functional in determining the structure of glassy $GeTe_4$. *Phys. Rev. B* **2015**, *92*, 134208. [CrossRef]
23. Luckas, J.; Olk, A.; Jost, P.; Volker, H.; Alvarez, J.; Jaffré, A.; Zalden, P.; Piarristeguy, A.; Pradel, A.; Longeaud, C.; et al. Impact of Maxwell rigidity transitions on resistance drift phenomena in Ge_xTe_{1-x} glasses. *Appl. Phys. Lett.* **2014**, *105*, 092108. [CrossRef]
24. Jóvári, P.; Piarristeguy, A.A.; Escalier, R.; Kaban, I.; Bednarcik, J.; Pradel, A. Short range order and stability of amorphous Ge_xTe_{100-x} alloys ($12 \leq x \leq 44.6$). *J. Phys. Condens. Matter* **2013**, *25*, 195401. [CrossRef] [PubMed]
25. Piarristeguy, A.A.; Micoulaut, M.; Escalier, R.; Jóvári, P.; Kaban, I.; van Eijk, J.; Luckas, J.; Ravindren, S.; Boolchand, P.; Pradel, A. Structural singularities in Ge_xTe_{100-x} films. *J. Chem. Phys.* **2015**, *143*, 074502. [CrossRef]
26. Piarristeguy, A.; Pradel, A.; Raty, J.-Y. Phase-change materials and rigidity. *MRS Bull.* **2017**, *42*, 45. [CrossRef]
27. Phillips, J.C. Topology of Covalent Non-Crystalline Solids I: Short-Range Order in Chalcogenide Alloys. *J. Non-Cryst. Solids* **1979**, *34*, 153. [CrossRef]
28. Thorpe, M.F. Continuous deformations in random networks. *J. Non-Cryst. Solids* **1983**, *57*, 355. [CrossRef]
29. Wright, A.C. Neutron and X-ray amorphography. *J. Non-Cryst. Solids* **1988**, *106*, 1. [CrossRef]
30. Elliot, S.R. Medium-range structural order in covalent amorphous solids. *Nature* **1991**, *354*, 445. [CrossRef]
31. Porod, G. *Small Angle X-Ray Scattering*; Glatter, O., Kratky, O., Eds.; Academic Press: London, UK, 1982; pp. 17–51, ISBN 0-12-286280-5.
32. Richard, D.; Ferrand, M.; Kearley, G.J. Analysis and Visualisation of Neutron-Scattering Data. *J. Neutron Res.* **1996**, *4*, 33. [CrossRef]
33. Sinha, S.K.; Sirota, E.B.; Stanley, H.B. X-ray and neutron scattering from rough surfaces. *Phys. Rev. B* **1988**, *38*, 2297. [CrossRef] [PubMed]
34. Salmon, P.S.; Martin, R.A.; Mason, P.E.; Cuello, G.J. Topological versus chemical ordering in network glasses at intermediate and extended length scales. *Nature* **2005**, *435*, 75. [CrossRef] [PubMed]